

Weak magnetic fields in central stars of planetary nebulae?*

M. Steffen¹, S. Hubrig¹, H. Todt², M. Schöller³, W.-R. Hamann², C. Sandin¹, and D. Schönberner¹

¹ Leibniz-Institut für Astrophysik Potsdam, An der Sternwarte 16, 14482 Potsdam, Germany

² Universität Potsdam, Institut für Physik und Astronomie, 14476 Potsdam, Germany

³ European Southern Observatory, Karl-Schwarzschild-Str. 2, 85748 Garching, Germany

Received March 19, 2014; accepted August 13, 2014

ABSTRACT

Context. It is not yet clear whether magnetic fields play an essential role in shaping planetary nebulae (PNe), or whether stellar rotation alone and/or a close binary companion, stellar or substellar, can account for the variety of the observed nebular morphologies.

Aims. In a quest for empirical evidence verifying or disproving the role of magnetic fields in shaping planetary nebulae, we follow up on previous attempts to measure the magnetic field in a representative sample of PN central stars.

Methods. We obtained low-resolution polarimetric spectra with FORS2 installed on the Antu telescope of the VLT for a sample of 12 bright central stars of PNe with different morphologies, including two round nebulae, seven elliptical nebulae, and three bipolar nebulae. Two targets are Wolf-Rayet type central stars.

Results. For the majority of the observed central stars, we do not find any significant evidence for the existence of surface magnetic fields. However, our measurements may indicate the presence of weak mean longitudinal magnetic fields of the order of 100 Gauss in the central star of the young elliptical planetary nebula IC418 as well as in the Wolf-Rayet type central star of the bipolar nebula Hen 2-113 and the weak emission line central star of the elliptical nebula Hen 2-131. A clear detection of a 250 G mean longitudinal field is achieved for the A-type companion of the central star of NGC 1514. Some of the central stars show a moderate night-to-night spectrum variability, which may be the signature of a variable stellar wind and/or rotational modulation due to magnetic features.

Conclusions. Since our analysis indicates only weak fields, if any, in a few targets of our sample, we conclude that strong magnetic fields of the order of kG are not widespread among PNe central stars. Nevertheless, simple estimates based on a theoretical model of magnetized wind bubbles suggest that even weak magnetic fields below the current detection limit of the order of 100 G may well be sufficient to contribute to the shaping of the surrounding nebulae throughout their evolution. Our current sample is too small to draw conclusions about a correlation between nebular morphology and the presence of stellar magnetic fields.

Key words. planetary nebulae: general – stars: magnetic fields – stars: AGB and post-AGB – binaries: close – techniques: polarimetric

1. Introduction

One of the major open questions regarding the formation of planetary nebulae (PNe) concerns the mechanism that is responsible for their non-spherical, often axisymmetric shaping (e.g., review by Balick & Frank 2002). Both central star binarity and stellar rotation in combination with magnetic fields are among the favorite explanations, but their role in PN formation and shaping is not yet sufficiently clear.

Basically, the origin of PNe is understood to be a consequence of the interaction of the hot central star with its circumstellar environment through photoionization and wind-wind collision. In the framework of this theory, the formation and evolution of PNe has been modeled in detail, assuming spherical symmetry (e.g., Marten & Schönberner 1991; Mellema 1994; Villaver et al. 2002; Perinotto et al. 2004; Steffen & Schönberner 2006) or axisymmetric geometry (e.g., Mellema 1995, 1997). The role of stellar rotation and magnetic fields in shaping PNe has been studied numerically in the pioneering work of García-Segura et al. (1999),

who find that most of the observed nebular morphologies can be modeled with an appropriate combination of input parameters. Magnetic shaping of PNe thus appears to be an attractive alternative to the popular binary hypothesis (e.g., De Marco 2009; Douchin et al. 2012). It remains unclear, however, whether the underlying assumptions of García-Segura et al. (constant stellar wind with a high magnetization parameter) are actually realistic, since very little is known so far about rotation rates and surface magnetic fields of the central stars of PNe.

The discovery of sufficiently strong magnetic fields in the central stars would lend considerable support to the hypothesis that the axisymmetric or bipolar appearance of many PNe is caused by magnetic fields (e.g., García-Díaz et al. 2008; Blackman 2009). On the other hand, theoretical arguments have been put forward to demonstrate that the structure of non-spherical planetary nebulae cannot be attributed to the presence of large scale magnetic fields, since they would contain more angular momentum and energy than a single star can supply (Soker 2006).

In principle, the role of magnetic fields in shaping PNe may be verified or disproved by empirical evidence, as already suggested by Jordan et al. (2005). Using FORS1 in

* Based on observations obtained at the European Southern Observatory, Paranal, Chile (ESO program No. 088.D-0425(A)).

Table 1. List of PNe central stars observed in the framework of our program, ordered by increasing RA.

(1) Name	(2) Catalog Identifier	(3) m_V	(4) Spectral type CSPN	(5) Companion ^{a)}	(6) Nebular morphology	(7) X-ray ^{b)} emission	References col. (4) col. (6)	
NGC 246	118.8-74.7	11.96	PG1159	G8-K0V	R	SP	1)	6)
NGC 1360 ^{*)}	220.3-53.9	11.35	sdO		E	SP	2)	6)
NGC 1514	165.5-15.2	9.42	–	A0III	E	HP		6)
IC 418	215.2-24.2	10.17	O7f		E	D	3)	6)
NGC 2346	215.6+03.6	11.47	–	A5V	B	N		7)
NGC 2392	197.8+17.3	10.53	O6f	dM?	E	HP, D	3)	6)
Hen 2-36	279.6-03.1	11.30	–	A2III	B	F		7)
LSS 1362 ^{*)}	273.6+06.1	12.47	sdO		E		4)	8)
NGC 3132	272.1+12.3	10.07	–	A2IV-V	E	N		6)
Hen 2-108	316.1+08.4	12.72	WELS		R		5)	6)
Hen 2-113	321.0+03.9	12.28	[WC11]		B	F	2), 5)	9)
Hen 2-131	315.1-13.0	11.01	WELS		E	F	2), 5)	6)

Notes. (2): Identification number from the Strasbourg Catalog of PNe; (3): Integrated V -band intensity of central star; (4): Spectral classification of central star ([WC11]: Wolf-Rayet type; WELS: weak emission line star, normal chemical composition); (5): Spectral classification of binary companion (A-type companions dominate the spectrum, spectral type of CSPN unknown); (6): Basic morphology of the planetary nebula, R (round), E (elliptical), B (bipolar); (7): X-ray classification, N (non-detection), SP (soft point source), HP (hard point source), D (diffuse source), F (future Chandra target);

^{*)}target analyzed by Jordan et al. (2005, 2012); ^{a)}De Marco (2009); ^{b)}Kastner et al. (2012);

¹⁾Werner & Herwig (2006); ²⁾Mendez & Niemela (1977); ³⁾Heap (1977); ⁴⁾Drilling (1983); ⁵⁾Tylenda et al. (1993);

⁶⁾Phillips (2003); ⁷⁾Corradi & Schwarz (1995); ⁸⁾Jordan et al. (2005); ⁹⁾Lagadec et al. (2006).

spectropolarimetric mode, they reported the detection of magnetic fields of the order of kG in the central stars of the PNe NGC 1360 and LSS 1362. A reanalysis of their data, however, did not provide any significant evidence for longitudinal magnetic fields in these stars that are stronger than a few hundred Gauss (Jordan et al. 2012). Their field measurements have typical error bars of 150 to 300 G. Similar results were achieved in the work of Leone et al. (2011), who concluded that the mean longitudinal magnetic fields in NGC 1360 and LSS 1362 are much weaker, less than 600 G, or that the field has a complex structure. The most recent search for magnetic fields in central stars of planetary nebulae by Leone et al. (2014), based on spectropolarimetric observations of 19 central stars with WHT/ISIS and VLT/FORS2, is partly affected by large measurement uncertainties and reports no positive detection either. Thus, convincing evidence for the presence of significant magnetic fields in the central stars of PNe is still missing.

Using low-resolution polarimetric spectra obtained with FORS2 installed at the Very Large Telescope, we carried out a search for magnetic fields in a sample of 12 central stars covering the whole range of morphologies from round to elliptical/axisymmetric, and bipolar PNe, and including both chemically normal and Wolf-Rayet (WR) type (hydrogen-poor) central stars. The sample includes two round nebulae (NGC 246, Hen 2-108), five elliptical nebulae (IC 418, NGC 1514, NGC 2392, NGC 3132, Hen 2-131), and three bipolar nebulae (NGC 2346, Hen 2-36, Hen 2-113). Two targets are WR-type central stars (NGC 246, Hen 2-113). In addition, we included the two (elliptical) targets of Jordan et al. (2005), NGC 1360 and LSS 1362, for which they originally claimed the detection of kG magnetic fields. Six of the 12 central stars are known binaries.

The data collected in our survey can provide a basis for further empirical investigations. Since our sample

comprises both normal hydrogen-burning, and Wolf-Rayet type (hydrogen-deficient) central stars, some insight may be gained into the physics of WR-type winds regarding the question of whether the much enhanced mass loss of [WC] type central stars (by a factor of ~ 100 with respect to the mass loss of normal central stars) is related to the presence of stellar magnetic fields.

Our target list includes a number of nebulae whose X-ray emission has been measured by Chandra and/or XMM Newton or are prospective targets in the Chandra PN Large Project (PI J. Kastner). In principle, our magnetic field measurements may help to answer the question why some central stars show up as X-ray point sources, while others, with similar stellar parameters, do not emit X-rays. The magnetic properties of the central stars and their winds could play an important role in this context. Similarly, the central cavity of some PNe is known to be a source of diffuse thermal X-ray emission, while other PNe are undetected in diffuse X-rays. Again, magnetic fields may be responsible: (i) sufficiently strong magnetic fields are expected to modify the thermal structure of the shock-heated stellar wind, and hence its X-ray emission, and (ii) even very weak magnetic fields suppress thermal conduction perpendicular to the field lines, with severe consequences for the X-ray luminosity and characteristic temperature (Steffen et al. 2008).

In Sect. 2, we give an overview of our observations and magnetic field measurements with VLT/FORS2, before we discuss the main results of our 12 targets in Sect. 3. Section 4 is devoted to theoretical estimates of the role of the central star's magnetic fields in PN shaping and of the influence of the magnetic fields on the diffuse X-ray emission of PNe. Finally, we summarize our main conclusions in Sect. 5.

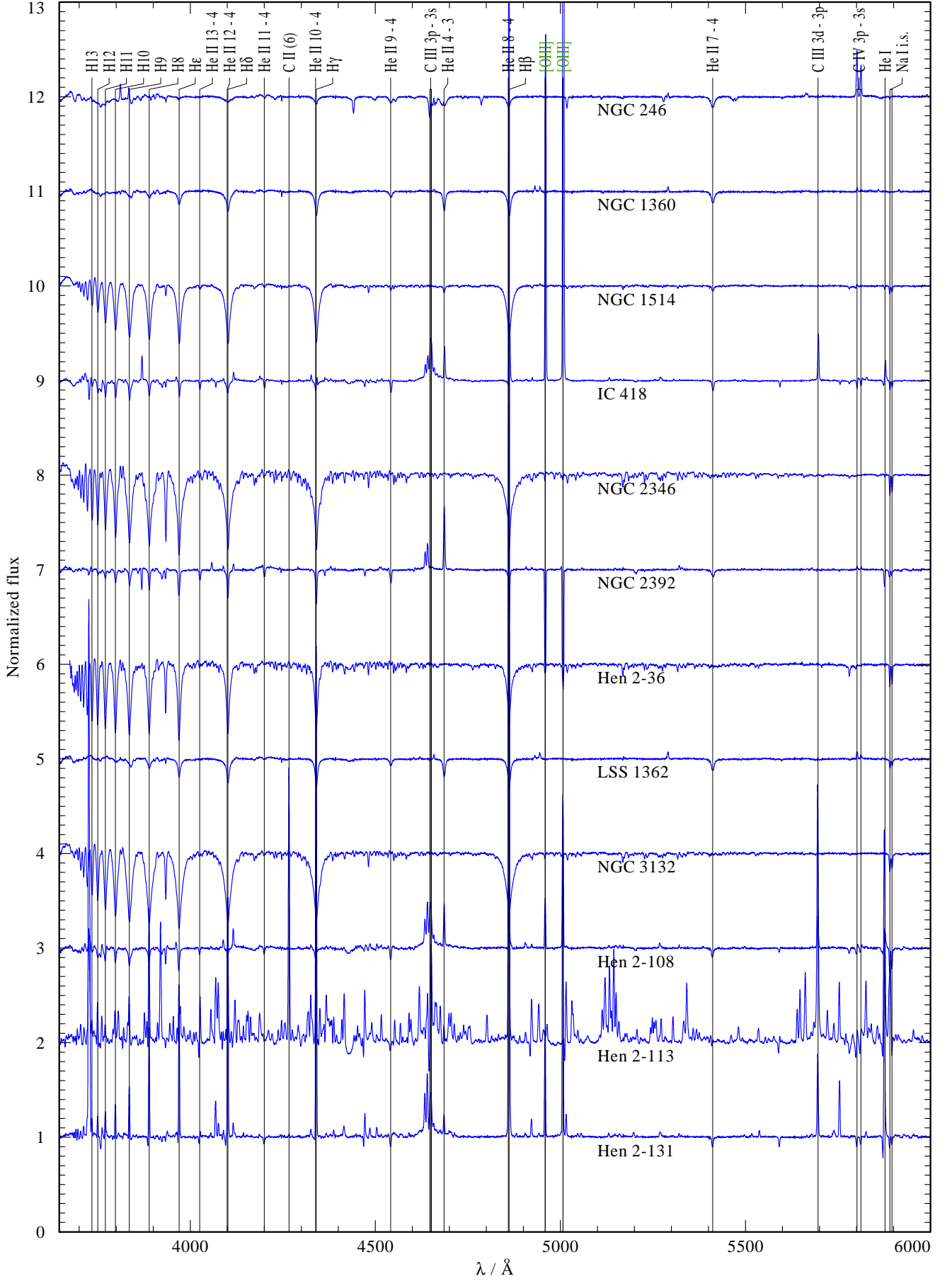


Fig. 1. Normalized FORS2 Stokes *I* spectra of the 12 central stars in our sample, displayed with a vertical offset of 1 unit between adjacent spectra. The strongest spectral lines are identified. The forbidden [O III] nebular emission lines close to 5000 Å are marked in green. They may appear in absorption (e.g., NGC 2392) due to imperfect background subtraction.

2. Observations and magnetic field measurements

Spectropolarimetric observations of 12 central stars were carried out from 2011 October 5 to 2012 March 28 in service mode at the European Southern Observatory with FORS 2 mounted on the 8-m Antu telescope of the VLT. Nine targets were observed twice, and three targets were observed three times. We present the list of targets in our sample in Table 1, where we also collect information about the spectral classification of the central stars, binarity, morphology of the nebulae, and observed X-ray emission.

The multi-mode instrument FORS 2 is equipped with polarization analyzing optics, comprising superachromatic halfwave and quarterwave phase retarder plates, and a Wollaston prism with a beam divergence of $22''$ in standard resolution mode. During the observations with FORS 2, we used a slit width of $0''.5$ and the GRISM 600B to achieve a spectral resolving power of about 1650.

From the raw FORS 2 data, the parallel and perpendicular beams are extracted using a pipeline written in the MIDAS environment by T. Szeifert, the very first FORS instrument scientist. This pipeline reduction by default includes background subtraction. A unique wavelength calibration frame is used for each night.

A first description of the assessment of the longitudinal magnetic field measurements using FORS 1/2 spectropolarimetric observations was presented in our previous work (e.g., Hubrig et al. 2004a, 2004b, and references therein). To minimize the crosstalk effect, a sequence of subexposures at the retarder position angles $-45^\circ + 45^\circ$, $+45^\circ - 45^\circ$, $-45^\circ + 45^\circ$, etc., is usually executed during observations and the V/I spectrum is calculated using:

$$\frac{V}{I} = \frac{1}{2} \left\{ \left(\frac{f^o - f^e}{f^o + f^e} \right)_{-45^\circ} - \left(\frac{f^o - f^e}{f^o + f^e} \right)_{+45^\circ} \right\} \quad (1)$$

where $+45^\circ$ and -45° indicate the position angle of the retarder waveplate and f^o and f^e are the ordinary and extraordinary beams, respectively. Rectification of the V/I spectra was performed in the way described by Hubrig et al. (2014). Null profiles, N , are calculated as pairwise differences from all available V profiles. From these, 3σ -outliers are identified and used to clip the V profiles. This removes spurious signals, which mostly come from cosmic rays and also reduces the noise. A full description of the updated data reduction and analysis will be presented in a separate paper (Schöller et al., in preparation).

The mean longitudinal magnetic field, $\langle B_z \rangle$, is measured on the rectified and clipped spectra based on the relation

$$\frac{V}{I} = -\frac{g_{\text{eff}} e \lambda^2}{4\pi m_e c^2} \frac{1}{I} \frac{dI}{d\lambda} \langle B_z \rangle, \quad (2)$$

where V is the Stokes parameter that measures the circular polarization, I is the intensity in the unpolarized spectrum, g_{eff} is the effective Landé factor, e is the electron charge, λ is the wavelength, m_e is the electron mass, c is the speed of light, $dI/d\lambda$ is the wavelength derivative of Stokes I , and $\langle B_z \rangle$ is the mean longitudinal (line-of-sight) magnetic field.

For the determination of the mean longitudinal stellar magnetic field, we consider two sets of spectral lines: (i) the entire spectrum including all available absorption and emission lines, apart from the usually strong [O III] nebula emission lines near 5000 \AA (in the following referred to as wavelength set *all*); and (ii) the subset of spectral lines

originating exclusively in the photosphere (and wind) of the central star and not appearing in the surrounding nebula spectrum (in the following wavelength set *star*), thus avoiding any potential contamination by nebular emission lines. This allows us to get an idea of the impact of the presence of nebula emission lines and the inclusion of the continuum windows on the magnetic field measurements. Details about the selected wavelength regions for the individual objects can be found in Appendix A.

Note that we do not differentiate between absorption and emission lines, since the relation between the Stokes V signal and the slope of the spectral line wing, as given by Eq. (2), holds for both type of lines, so that the signals of emission and absorption lines add up rather than cancel. For simplification, we assume a typical Landé factor of $g_{\text{eff}} \approx 1.2$ for all lines.

Given the Stokes I and Stoke V spectra of the selected wavelength region, the mean longitudinal magnetic field $\langle B_z \rangle$ is derived by linear regression employing two different methods, in the following referred to as method R1 and RM.

In *method R1*, $\langle B_z \rangle$ is defined by the slope of the weighted linear regression line through the measured data points, where the weight of each data point is given by the squared signal-to-noise ratio of the Stokes V spectrum. The formal 1σ error of $\langle B_z \rangle$ is obtained from the standard relations for weighted linear regression. This error is inversely proportional to the rms signal-to-noise ratio of Stokes V . Finally, the factor $\sqrt{\chi^2_{\text{min}}/\nu}$ is applied to the error determined from the linear regression, if larger than 1 (for details see Appendix B.1).

In *method RM*, we generate $M = 10^6$ statistical variations of the original dataset by the bootstrapping technique, and analyze the resulting distribution $P(\langle B_z \rangle)$ of the M regression results. Mean and standard deviation of this distribution are identified with the most likely mean longitudinal magnetic field and its 1σ error, respectively. The main advantage of this method is that it provides an independent error estimate (see Appendix B.2).

Normalized FORS 2 Stokes I spectra of all sample stars (averaged over the different epochs) are displayed in Fig. 1; line identifications of well-known spectral lines are listed at the top. The appearance of the spectra already provides a clue of the binarity status of the central stars: the spectra of NGC 1514, NGC 2346, Hen 2-36, and NGC 3132 are largely dominated by companions of spectral type A. The spectra of the central stars Hen 2-131 and Hen 2-113, and to a lesser extent Hen 2-108, predominantly show emission lines, whereas the remaining central stars show a predominance of absorption lines.

The results of our stellar magnetic field measurements are presented in Table 2. For each object and each observing night, the mean longitudinal magnetic field, as derived from methods R1 and RM, is listed for both sets of lines (*all* and *star*). The mean longitudinal magnetic field derived from the original dataset with method R1 is always close to the result obtained with the Monte-Carlo method RM, $\langle B_z \rangle$. Moreover, the 1σ uncertainties obtained from method R1 (Eq. B.4) and method RM (Eq. B.9), respectively, agree remarkably well. No significant fields were detected in the null spectra calculated using the formalism described by Bagnulo et al. (2012).

Table 2. Longitudinal magnetic field measurements of the central stars in our sample, with the modified Julian date of mid-exposure given in Col. (2). The mean longitudinal magnetic field measured with method R1 (regression based on a single dataset) using the entire spectrum (*all*) and using only the uncontaminated stellar lines (*star*), respectively, is presented in Cols. (3) and (5). The corresponding results based on method RM (regression based on $M = 10^6$ statistical variations of the original dataset) are shown in Cols. (4) and (6). The average signal-to-noise ratio of the stacked Stokes I spectrum is given in Col. (7). A magnetic field detection at a significance level of 3σ is indicated by the bold face entries in Cols. (3) – (6). All quoted errors are 1σ uncertainties.

Name	MJD	$\langle B_z \rangle_{\text{all}}$ [G]		$\langle B_z \rangle_{\text{star}}$ [G]		S/N	Notes
		R1	RM	R1	RM		
NGC 246	55843.1712	-25 ± 90	-21 ± 79	-55 ± 93	-51 ± 78	1665	
	55859.1612	62 ± 77	62 ± 75	66 ± 79	66 ± 76	1369	
NGC 1360	55839.2227	-7 ± 97	-7 ± 92	78 ± 142	79 ± 129	2161	
	55843.3429	-109 ± 145	-104 ± 134	-192 ± 207	-183 ± 207	1952	
NGC 1514	55844.3521	138 ± 94	139 ± 88	122 ± 94	123 ± 89	2035	A-star
	55859.2523	-256 ± 85	-257 ± 77	-252 ± 85	-252 ± 77	2202	:
IC 418	55840.2816	only two sub-exposures, no measurement of $\langle B_z \rangle$					
	55879.3257	-181 ± 54	-177 ± 54	-204 ± 97	-201 ± 101	1870	
	55899.1557	-157 ± 64	-157 ± 57	-143 ± 87	-143 ± 83	1733	
NGC 2346	55885.2538	-44 ± 74	-41 ± 88	-31 ± 104	-24 ± 124	1264	A-star
	55905.3067	-86 ± 45	-86 ± 44	-54 ± 59	-53 ± 60	1860	:
	55906.2222	-82 ± 62	-82 ± 60	-23 ± 68	-23 ± 65	1723	:
NGC 2392	55917.2243	46 ± 73	46 ± 78	-132 ± 152	-135 ± 145	1612	
	55926.2776	137 ± 81	136 ± 87	219 ± 163	224 ± 133	1635	
Hen 2-36	55906.2864	-116 ± 74	-116 ± 69	-107 ± 97	-107 ± 93	1641	A-star
	55908.3180	-99 ± 92	-99 ± 94	-70 ± 111	-69 ± 113	1434	:
LSS 1362	55909.2720	38 ± 236	35 ± 234	157 ± 263	152 ± 264	985	
	55917.3188	-95 ± 175	-91 ± 177	-105 ± 208	-101 ± 208	1163	
NGC 3132	55909.3216	38 ± 70	38 ± 70	97 ± 86	97 ± 87	1610	A-star
	55924.2987	65 ± 51	65 ± 60	74 ± 62	73 ± 76	2030	:
Hen 2-108	55981.2533	261 ± 126	253 ± 135	374 ± 179	351 ± 213	881	
	55996.2235	-118 ± 142	-115 ± 121	-274 ± 220	-280 ± 218	882	
	56014.3206	-12 ± 121	-1 ± 140	98 ± 201	115 ± 175	804	
Hen 2-113	55981.3145	-58 ± 18	-58 ± 24	-78 ± 25	-80 ± 26	1236	
	55996.2851	-51 ± 18	-51 ± 21	-47 ± 24	-47 ± 30	1316	
Hen 2-131	55996.3520	-92 ± 29	-90 ± 41	-109 ± 41	-107 ± 50	1972	
	55997.3157	-120 ± 32	-119 ± 50	-90 ± 39	-89 ± 51	1936	

Considering the entire spectrum (wavelength set *all*), we achieve formal 3σ detections for NGC 1514 (second night) and IC 418 (second night) with both methods (R1 and RM), and for the WR-type central star Hen 2-113 and the ‘weak emission line star’ (WELS) Hen 2-131 with method R1 only. Repeating the magnetic field measurements on the restricted wavelength range with clean stellar lines only (wavelength set *star*), formal 3σ detections are confirmed in the case of NGC 1514 (second night) and Hen 2-113 (first night). For IC 418 and Hen 2-131, the $\langle B_z \rangle$ values found from wavelength sets *all* and *star* are very similar, but the formal errors are larger in the latter case, resulting in 2σ detections only.

NGC 1514 is the only object where we detect a magnetic field consistently with both methods and with both sets of lines above the 3σ significance level, indicating a mean longitudinal field of ≈ 250 G on the second night. Note, however, that in NGC 1514 the spectrum of the central star is dominated by an A-type companion, such that we only measure the magnetic field of the A-type star, while

the magnetic field of the hot, compact central star proper remains inaccessible.

The magnetic field detection in the WR-type central star Hen 2-113 is significant above the 3σ level with both R1 and RM when considering clean stellar lines only. However, the detected magnetic field is very weak, $\langle B_z \rangle \approx 80$ G.

In the following section, we discuss the individual targets of our sample in more detail.

3. Individual targets: general information, spectral variability, magnetic field detection, X-rays

For all our targets, the basic data of the central stars and their nebulae, as collected from the literature, are summarized in Tables 1 and 3, together with related references. For most of the targets, additional information may be found in Table 1 of Kastner et al. (2012).

NGC 246: The hot central star ($T_{\text{eff}} \approx 150$ kK) belongs to the group of PG 1159 stars, which are hot hydrogen deficient post-AGB stars (e.g., Werner & Herwig 2006). In the Hertzsprung-Russell diagram, they cover a region comprising the hottest central stars of planetary nebulae and white dwarfs ($T_{\text{eff}} = 75$ to 200 kK, $\log g = 5.5$ to 8.0). Their H deficiency is most probably the result of a late He-shell flash. Their envelopes are mainly composed of He, C, and O, with rather diverse abundance patterns (mass fractions: He = 0.30 to 0.85, C = 0.13 to 0.60, O = 0.02 to 0.20).

The projected rotational velocity of the central star was determined spectroscopically by Rauch et al. (2003) as $v \sin i = 77_{-17}^{+23}$ km/s. NGC 246 is a round planetary nebula whose central star is a known visual binary, with a companion of spectral type G8-K0 V (e.g., De Marco 2009). Chandra observations revealed a central point source of soft X-rays (for details see Hoogerwerf et al. 2007).

We observed this central star on two different nights, without detecting any spectral variability in the FORS 2 spectra. No magnetic field was detected on either night. The error estimates of both methods (R1 and RM) are in good agreement, yielding $\sigma_B \lesssim 100$ G, irrespective of the wavelength set considered for the magnetic field measurement. Hence, the 3σ upper limit for the mean longitudinal magnetic field is roughly $|\langle B_z \rangle| \lesssim 300$ G.

NGC 1360: The central star of this elliptical PN has recently been analyzed by Herald & Bianchi (2011). According to this study, the mass loss rate is the lowest of all central stars of our sample (see Tab. 3). Kastner et al. (2012) find this central star to be a point source of soft X-rays.

Based on spectropolarimetric data obtained with FORS 1, Jordan et al. (2005) reported the detection of a magnetic field of the order of several kG. Leone et al. (2011, 2014) re-observed the central star with FORS 2, but could not confirm the presence of a magnetic field within an uncertainty of ~ 100 G. Later on, Jordan et al. (2012) reanalyzed their own data and concluded that no magnetic field is present in this star. Our observations with FORS 2 on two different nights with an uncertainty ≈ 150 G are fully in agreement with these recent works. The 3σ upper limit for the mean longitudinal magnetic field is $|\langle B_z \rangle| \lesssim 450$ G.

NGC 1514: The spectrum of the central star is largely dominated by a companion of spectral type A0 III (e.g., De Marco 2009). Recent Chandra observations revealed that this elliptical PN harbors a central point source of hard X-rays (Kastner et al. 2012).

The inspection of our Stokes I spectra obtained on two different nights indicates a very low, if not negligible, spectral variability.

On the first night, no significant magnetic field is detectable ($\langle B_z \rangle \approx 130 \pm 90$ G). For the second epoch, however, the magnetic field measurements showed a detection of a longitudinal field of negative polarity at a 3σ significance level ($\langle B_z \rangle = -250 \pm 80$ G), using the clean stellar lines only. The results obtained from methods R1 and RM are fully consistent, as illustrated in Fig. 2: the top panel shows the linear regression plot of method R1, V/I versus $-(g_{\text{eff}} e \lambda^2)/(4\pi m_e c^2) I^{-1} dI/d\lambda$, where the slope represents $\langle B_z \rangle$, while the bottom panel displays the distribu-

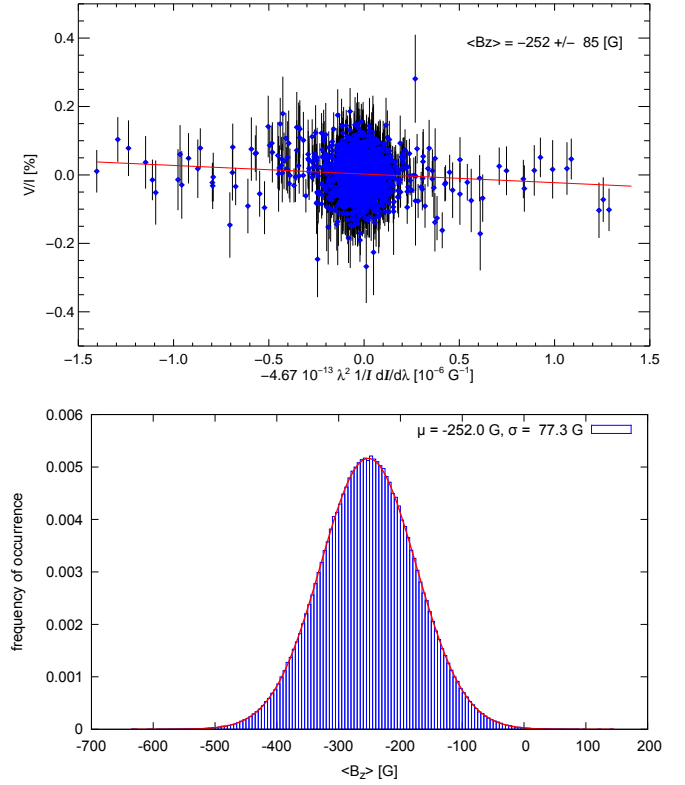


Fig. 2. NGC 1514: Regression detection of a magnetic field on the second night, using uncontaminated stellar lines only. Methods R1 and RM yield a mean longitudinal magnetic field of $\langle B_z \rangle = -252 \pm 85$ G (top) and $\langle B_z \rangle = -252 \pm 77$ G (bottom), respectively. In the bottom panel, and the following figures of this kind, the histogram plot has a bin size of 5 G, and the (red) curve represents a Gaussian with the same mean value and standard deviation as the histogram data.

tion of $\langle B_z \rangle$ as obtained with method RM. We find similar results for the magnetic field if we perform our analysis on the entire spectrum, which is not surprising, however, since there are only a few nebular emission lines that contaminate the stellar spectrum.

Based on this clear detection, the lower limit of the magnetic field strength is $|\langle B_z \rangle| \gtrsim 250$ G. However, the field must be assigned to the A-type companion of the central star proper.

IC 418: The central star of this young, elliptical planetary nebula was analyzed extensively (see, e.g., Mendez et al. 1988, 1992; Kudritzki et al. 1997, 2006; Pauldrach et al. 2004; Morisset & Georgiev 2009). The nebula is listed as a source of diffuse X-ray emission in Table 1 of Kastner et al. (2012). A more detailed recent analysis of the X-ray properties of IC 418 is listed in Ruiz et al. (2013). The projected rotational velocity of the central star was recently determined from a Fourier transform analysis of photospheric lines by Prinja et al. (2012), who found $v \sin i = 56$ km/s.

Spectropolarimetric observations of the central star were carried out on three different nights. A significant spectral variability is detected in the He II lines at $\lambda 4541$ and 5412 \AA and in the C IV lines near $\lambda 5800 \text{ \AA}$. Note that these lines appear not to be blended with nebular emission

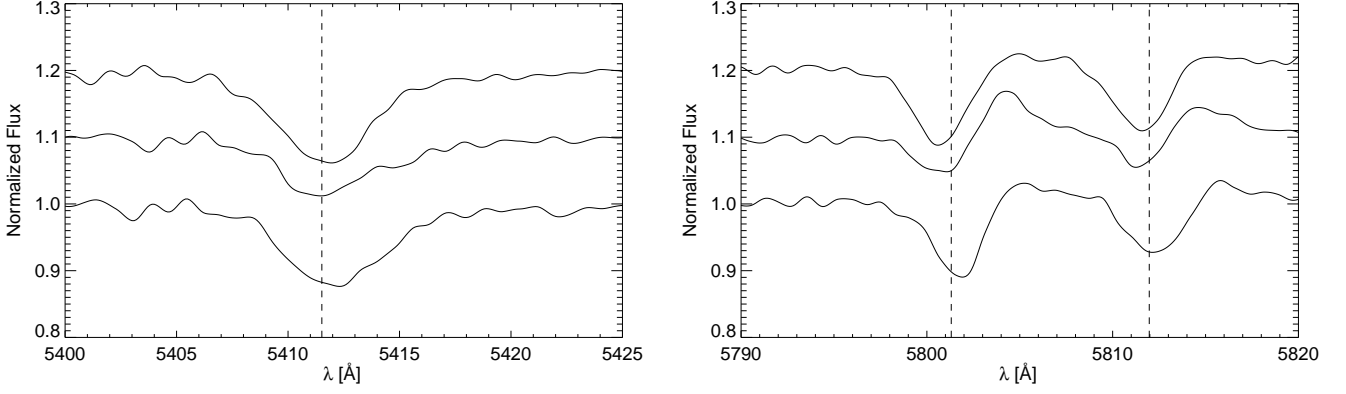


Fig. 3. IC 418: Normalized Stokes I spectra of the central star in the spectral regions around the He II line at λ 5411.5 Å (left) and the C IV lines λ 5801.3 and 5812.0 Å (right) obtained on three different nights. The spectra are shifted in vertical direction by 0.1 units for clarity, with the epoch increasing from bottom to top (the ordinate is correct for the lowermost spectrum).

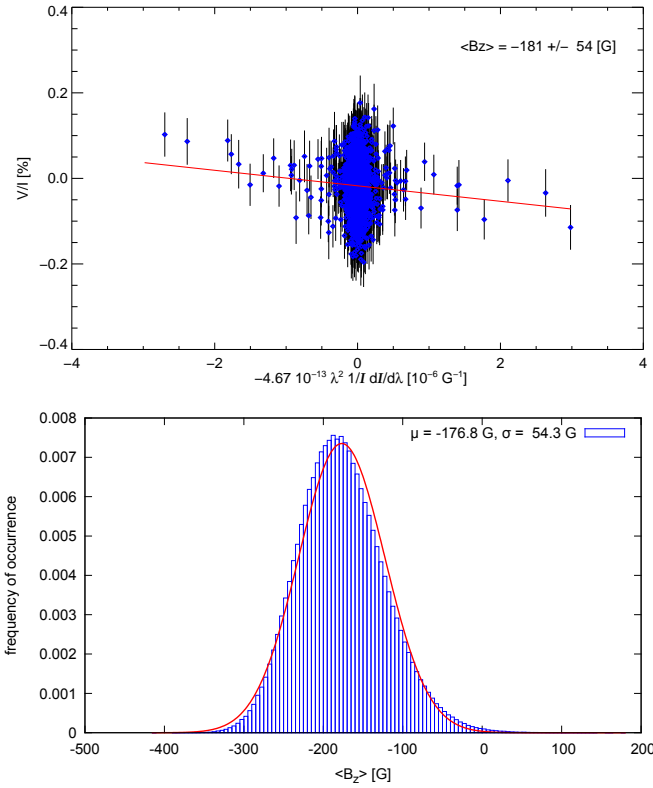


Fig. 4. IC 418: Regression detection with method R1 of a $\langle B_z \rangle = -181 \pm 54$ G mean longitudinal magnetic field on the second night, using all lines (top). The corresponding $\langle B_z \rangle$ distribution obtained from method RM (bottom) deviates from a Gaussian (red curve) and indicates $\langle B_z \rangle = -177 \pm 54$ G.

lines (see also Fig. 1 of Mendez et al. 1988). In Fig. 3, we present as an example the variability of the He II line at λ 5412 Å and of the C IV line profiles near λ 5800 Å.

A mean longitudinal magnetic field of negative polarity was detected at the 3σ level of significance on the second night when using the entire spectrum: $\langle B_z \rangle = -181 \pm 54$ G (method R1) and $\langle B_z \rangle = -177 \pm 54$ G (method RM), as shown in Fig. 4. The results obtained from both methods are essentially identical. However, when using the uncon-

taminated stellar lines only, the formal error increases to $\sigma_B \approx 100$ G, and we are left with a 2σ signal in this case. It is noteworthy that all measurements for this object fall in the narrow range 175 ± 30 G. Nevertheless, adopting 100 G as the valid error estimate, the magnetic field detection in IC 418 must be considered as marginal and we infer a conservative 3σ upper limit for the mean longitudinal magnetic field of $|\langle B_z \rangle| \lesssim 300$ G.

NGC 2346: The optical spectrum of the central star of this bipolar PN is largely dominated by a companion of spectral type A5 V (e.g., De Marco 2009). The inspection of the Stokes I spectra obtained on three different nights indicates a very low spectral variability, as in the case of NGC 1514. Higher resolution spectra would be needed to establish a possible low-amplitude variability of the A-type stellar spectrum.

None of our spectropolarimetric measurements indicates the presence of a magnetic field signal. We conclude that the mean longitudinal magnetic field of the A-type companion, $|\langle B_z \rangle|$, does not exceed 300 G.

According to Kastner et al. (2012), neither the central star (wind) nor the central cavity of the PN shows detectable X-ray emission.

NGC 2392: The spectrum of the central star of this round/elliptical PN was analyzed extensively (see, e.g., Mendez et al. 1988, 1992; Kudritzki et al. 1997, 2006; Pauldrach et al. 2004). According to Kastner et al. (2012), the central cavity of the nebula is a source of diffuse X-ray emission and, in addition, harbors a hard X-ray point source. A more detailed recent analysis of the X-ray properties of NGC 2392 is presented by Ruiz et al. (2013). Possibly, the central star has a late-type (dM) companion (Ciardullo et al. 1999).

No significant line profile variability is detected, neither in the Stokes I nor in the Stokes V spectra. Similarly, no significant magnetic field signal was detected on either observing night. Typical 1σ errors are ≈ 80 G when the entire spectrum is used, and ≈ 150 G when only the clean stellar lines are considered for the magnetic field measurement. A conservative 3σ upper limit for the mean longitudinal

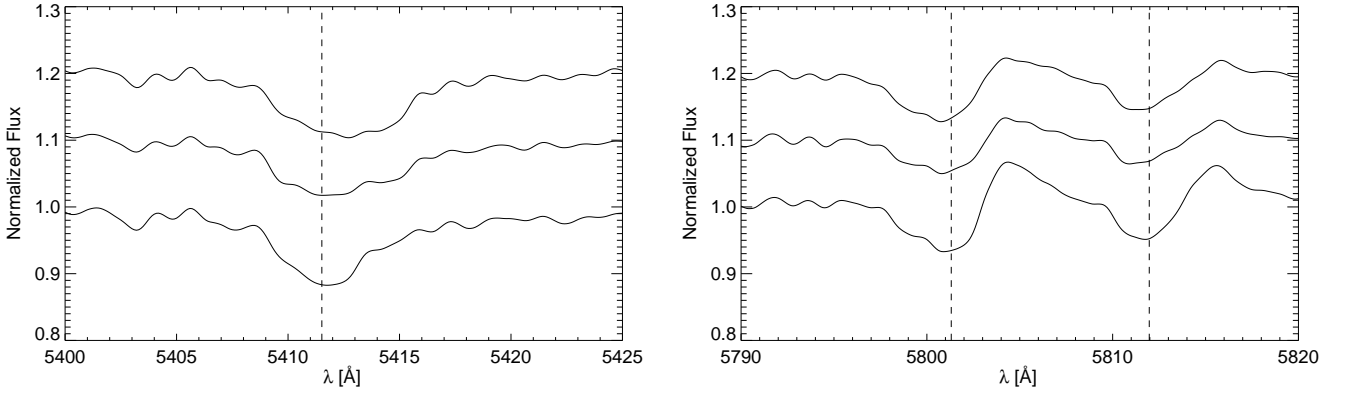


Fig. 5. Hen 2-108: Normalized Stokes I spectra of the central star of the round planetary nebula in the spectral regions around the He II line at λ 5411.5 Å (left) and the C IV doublet at λ 5801.3 and 5812.0 Å (right) obtained on three different nights. The spectra are shifted in vertical direction by 0.1 units for clarity, with the epoch increasing from bottom to top.

magnetic field of the central star of NGC 2392 is therefore $|\langle B_z \rangle| \lesssim 450$ G.

Hen 2-36: The optical spectrum of the central star of this bipolar PN is largely dominated by a companion of spectral type A. Spectral variability is very weak in both Stokes I and Stokes V spectra. Our measurements on two different observing nights show no evidence for the presence of a magnetic field in the central star of Hen 2-36, neither with method R1 nor with method RM, and irrespective of the considered spectral range. With typical errors of $\sigma_B \approx 100$ G, we estimate a 3σ upper limit of $|\langle B_z \rangle| \lesssim 300$ G.

LSS 1362: Using spectropolarimetric data obtained with FORS1, Jordan et al. (2005) reported the detection of a magnetic field of the order of several kG. Leone et al. (2011, 2014) reobserved the central star with FORS2 but, similar to the case of NGC 1360, the authors could not confirm the presence of a magnetic field within an uncertainty of ~ 290 G. Likewise, Jordan et al. (2012) reanalyzed their own data and concluded that no magnetic field is detectable in this star. As with NGC 1360, our observations with FORS2 on two different nights, with an uncertainty of about 300 G, do not indicate the presence of a magnetic field, in full agreement with these two recent works. A conservative 3σ upper limit for the mean longitudinal field of this central star is estimated to be $|\langle B_z \rangle| \lesssim 800$ G.

NGC 3132: The optical spectrum of the central star of this elliptical PN is largely dominated by a companion of spectral type A2 IV-V (e.g., De Marco 2009). The inspection of the Stokes I spectra obtained on two different nights indicates a very low spectral variability, as in the other targets with A-type companions.

No significant ($\gtrsim 3\sigma$ for both sets of lines) mean longitudinal magnetic field was measured on either night, even though the error estimates of both methods (R1 and RM) are less than 100 G. The estimated 3σ upper limit for the mean longitudinal magnetic field of the A star companion is therefore relatively low, $|\langle B_z \rangle| \lesssim 270$ G.

No X-ray detection is reported for NGC 3132 by Kastner et al. (2012), neither from the planetary nebula nor from its central star.

Hen 2-108: The spectrum of the central star of this round PN appears very similar to that of IC 418 (cf. Fig. 1, and Fig. 1 of Mendez et al. 1988). According to Tyllenda et al. (1993), the central star of Hen 2-108 is a weak emission line star (WELS). Such stars have normal chemical composition, but show narrow lines from the λ 4650 N III–C III–C IV blend and the C IV λ 5806 doublet; C III λ 5696 is absent or weak, while He II λ 4686 emission is often seen. These lines are also seen in some massive O-type stars, low-mass X-ray binaries, and cataclysmic variables. Further analyses of the central star can be found in Mendez et al. (1988, 1992) and Pauldrach et al. (2004). No information is available concerning the X-ray emission of this PN.

The Stokes I spectra show some variability, as demonstrated in Fig. 5, where we display the variable *stellar* line profiles of He II λ 5412 Å and the C IV lines near λ 5800 Å. However, we do not detect any mean longitudinal magnetic field at a significance level of 3σ on any of the three nights, irrespective of the adopted method and set of lines. Accepting the larger error estimates derived with the restricted wavelength set *star*, we obtain a conservative 3σ upper limit for the mean longitudinal field of this central star of $|\langle B_z \rangle| \lesssim 700$ G.

Hen 2-113: The central star of this bipolar PN is H-deficient, classified as a Wolf-Rayet star of type [WC11] (Mendez & Niemela 1977; Tyllenda et al. 1993). Hen 2-113 was not yet observed by the *Chandra* X-ray Observatory, and no other information is available concerning the X-ray emission of this PN.

The target Hen 2-113, with a rich emission line spectrum, shows a variable slope of the continuum in Stokes V spectra obtained at different epochs. Such variable continuum slopes were previously detected in our measurements of a few Herbig Ae stars with complex circumstellar environment, a few WR stars, and in the magnetic Of?p star HD 148937, which is surrounded by the circumstellar nebula NGC 6164-65 that expands with a projected velocity of about 30 km/s (Leitherer & Chavarria 1987). The Stokes V

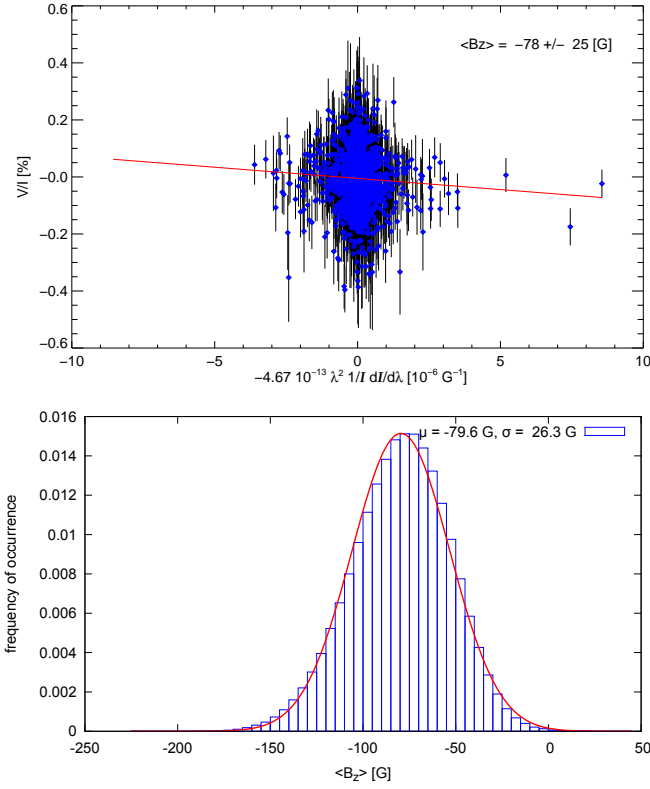


Fig. 6. Hen 2-113: Regression detection of a $\langle B_z \rangle = -78 \pm 25$ G mean longitudinal magnetic field on the first night with method R1, using uncontaminated stellar lines only (top), and corresponding (slightly non-Gaussian) distribution of $\langle B_z \rangle$ obtained from method RM (bottom).

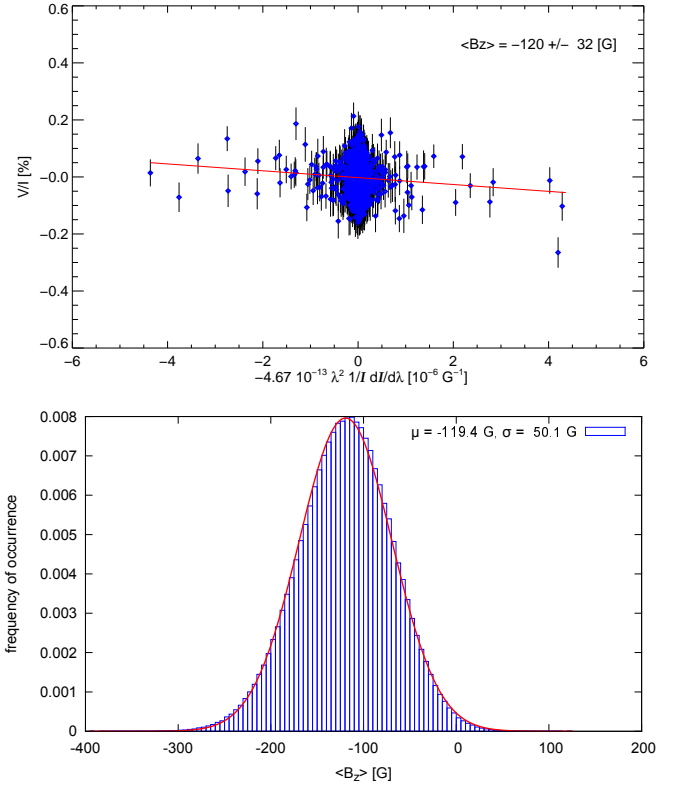


Fig. 8. Hen 2-131: Regression detection of a $\langle B_z \rangle = -120 \pm 32$ G mean longitudinal magnetic field with method R1, using the entire spectrum (top), and corresponding distribution of $\langle B_z \rangle$ derived from method RM (bottom).

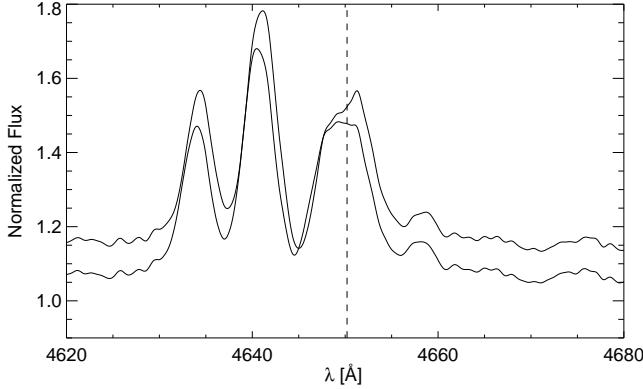


Fig. 7. Hen 2-131: Normalized Stokes I spectra of the central star in the spectral region around the C III feature at $\lambda 4650.2 \text{ \AA}$, obtained on two different nights. The spectrum of the second night is shifted upward in vertical direction by 0.1 units for clarity.

spectra for Hen 2-113 were rectified before the magnetic field measurements were made.

A weak, but significant mean longitudinal magnetic field of negative polarity was detected with both method R1 and RM on the first observing night: $\langle B_z \rangle = -58 \pm 18$ G and $\langle B_z \rangle = -58 \pm 24$ G, respectively, when using the entire spectrum (wavelength set *all*), and $\langle B_z \rangle = -78 \pm 25$ G and $\langle B_z \rangle = -80 \pm 26$ G, respectively, when using the clean stellar lines only (wavelength set *star*). The latter detection is

illustrated in the top panel of Fig. 6. Note that the formal error of the linear regression is particularly small in this case, mainly because the spread of the data points in x is large (cf. Eq. B.4) due to the presence of sharp emission lines (large $dI/d\lambda$). As before, methods R1 and RM provide essentially the same error estimates, suggesting that the detection is solid.

In the case of Hen 2-113, we have derived another independent error estimate based on an experiment with simulated data (see Appendix C). This experiment shows that, under somewhat idealized conditions, our analysis method is expected to have a typical 1σ error of about 35 G, given the spectral resolution and signal-to-noise ratio of the present observations. This error estimate is somewhat larger than those reported above from methods R1 and RM. We speculate that this mismatch may be related to the fact that the number of lines in the synthetic spectrum is lower than in the observed spectrum. Nevertheless, the numerical experiment with synthetic spectra indicates that the errors obtained from the actual measurements in the range $\sigma_B = 18$ to 30 G are not unrealistic, and that the 3σ detection limit of our present measurements of Hen 2-113 is as low as $|\langle B_z \rangle| \approx 120$ G.

Hen 2-131: According to Tyndenda et al. (1993) the central star is a weak emission line star (WELS). No information is available concerning the X-ray emission of this elliptical planetary nebula.

The Stokes I spectra appear to be variable. In Fig. 7 we present as an example the C III $\lambda 4650.2$ line profile vari-

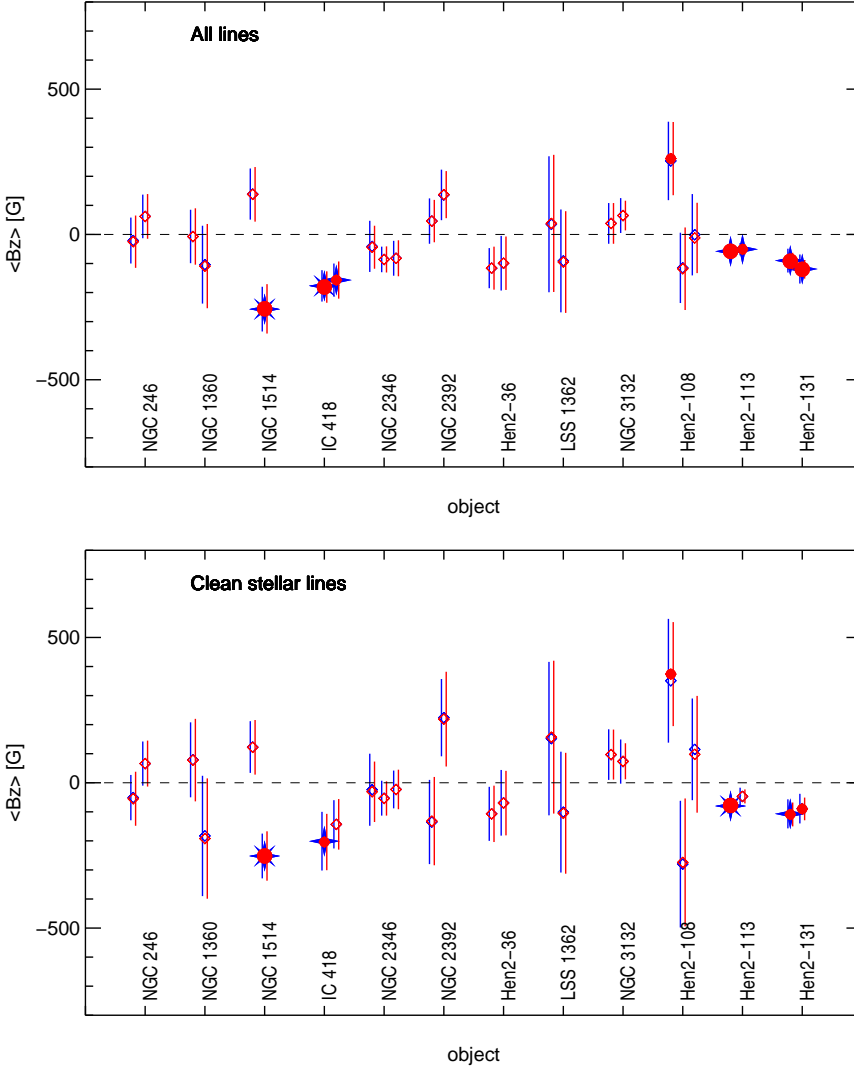


Fig. 9. Summary of our magnetic field measurements for the 12 targets of our sample, using wavelength set *all* (entire spectrum, top) and wavelength set *star* (clean stellar lines only, bottom) as listed in Table 2. Open symbols indicate non-detections, small and large filled dots (red) stand for 2σ and 3σ detections, respectively, with method R1, while (blue) stars mark 2σ (4 rays) and 3σ (8 rays) detections with method RM. Error bars refer to 1σ errors from method R1 (red) and RM (blue), respectively.

ability detected in the Stokes I spectra obtained on both observing nights.

Relying on method R1, and using the entire spectrum, a weak mean longitudinal magnetic field was detected on both observing nights at a formal significance level of $\gtrsim 3\sigma$: $\langle B_z \rangle = -92 \pm 29$ G and $\langle B_z \rangle = -120 \pm 32$ G, on the first and second night, respectively. The latter detection is illustrated in Fig. 8 (top). Relying instead on method RM, we obtain very similar magnetic field strengths, but slightly larger error bars: $\langle B_z \rangle = -90 \pm 41$ G and $\langle B_z \rangle = -119 \pm 50$ G (Fig. 8, bottom). Similar results are derived when using the clean stellar lines only, again indicating a mean longitudinal magnetic field of ≈ -100 G, but only with a significance of 2σ . Hen 2-131 may thus be a marginal detection.

The 3σ upper limit for the mean longitudinal field of this central star is as low as $|\langle B_z \rangle| \lesssim 150$ G.

4. Discussion

4.1. Significance of our magnetic field measurements

Most of the stars of our sample were not studied at the achieved accuracy before, and the present study allows us to put further constraints on the strength of the magnetic

fields in central stars of planetary nebulae. In Fig. 9 we present a synopsis of the results of our magnetic field measurements based on the entire spectrum (top) and on clean stellar lines only (bottom).

The achievable measurement accuracy is limited by the comparatively low number of useful spectral lines for the magnetic field diagnostics in the central stars of planetary nebulae. In addition, since no linear polarization measurements exist for our sample stars, it is difficult to assess how our detections are affected by crosstalk. It is therefore challenging to provide reliable estimates for $\langle B_z \rangle$.

In addition to the formal errors from the linear regression (method R1, Appendix B.1), we have alternatively considered an independent error estimate obtained from a bootstrapping analysis (method RM, Appendix B.2). As may be seen from Fig. 9, the errors from method RM turn out to be surprisingly similar to those from method R1. This close agreement suggests that our error estimates can be considered realistic.

If we require that a detection is only valid if it is found with both method R1 and method RM when using the wavelength set *star* (clean stellar lines only), then we count two 3σ detections, namely NGC 1514 (second night) and Hen 2-113 (first night), and two cases where our measure-

Table 3. Physical parameters of the central stars of the PNe observed in the present program (excluding those whose spectra are outshone by an A-type companion). The quantity $|3 \langle B_z \rangle|$ is the upper limit of the surface magnetic field derived from our measurements and B_s^* and B_s^\dagger is the minimum magnetic field strength at the stellar surface that would be required to shape the nebula according to Eq. (4) and (5), respectively.

Name	T_{eff} [kK]	R_s [R_\odot]	$\log(L/L_\odot)$	d [kpc]	$\log \dot{M}$ [M_\odot/yr]	v_w [km/s]	v_{rot}^a [km/s]	$ 3 \langle B_z \rangle $ [G]	B_s^* [G]	B_s^\dagger [G]	Ref. cols. (2)–(8)
NGC 246	150	0.20	4.20	0.50	−6.90	3500	>77	< 900	1500	2.3×10^5	5,7,9
NGC 1360	97	0.30	3.64	0.93	−10.60	1250	~10	< 1350	23	1210	2,3
IC 418	39	1.59	3.72	1.20	−7.50	700	>56	< 900	12	62	1,8
NGC 2392	45	1.34	3.82	1.28	−8.10	300	~10	< 1350	11	83	1
LSS 1362	114	0.18	3.70	1.03	−8.70	2400	~10	< 2400	920	7.2×10^4	2,3
Hen 2-108	34	2.60	3.92	5.80	−6.85	700	~10	< 2100	85	320	4
Hen 2-113	31	2.50	3.72	1.23	−6.10	160	~10	< 360	23	68	6
Hen 2-131	32	3.50	4.07	3.30	−6.88	400	~10	< 450	26	85	4

Notes. References: (1) Ruiz et al. (2013); (2) Traulsen et al. (2005); (3) Herald & Bianchi (2011); (4) Kudritzki et al. (2006); (5) Koesterke et al. (1998); (6) De Marco & Crowther (1998); (7) Bond & Ciardullo (1999); (8) Prinja et al. (2012); (9) Rauch et al. (2003). ^{a)} Assuming $v_{\text{rot}} = 10$ km/s where no measurements are available.

ments indicate a magnetic field at the 2σ significance level, namely IC 418 (second night) and Hen 2-131 (first night). IC 418 is, in fact, a 3σ detection with wavelength set *all*. For the two emission line objects Hen 2-113 and Hen 2-131, the formal error is remarkably small, in the case of Hen 2-113 even smaller than the theoretical estimate derived from numerical experiments with synthetic spectra (Appendix C), and hence these formal detections must be considered with some caution.

In all cases, the magnetic field is detected only during one out of two useful observing nights, which, in view of the expected rotation periods of only a few days, might be attributed to rotational modulation by large-scale magnetic structures.

In summary, we cannot claim a clear positive detection of a magnetic field in any of the PN central stars of our sample. What we can do, though, is to estimate individual upper limits of $|3 \langle B_z \rangle|$, as set by the quality of our measurements and the sensitivity of our analysis method (see Table 3, Col. 9). In the following, we investigate whether such upper limits are sufficient to rule out the PN magnetic shaping scenario.

4.2. The magnetized stellar wind

If large-scale (dipole-like) magnetic fields are present at the surface of a central star, they are carried along with the fast stellar wind and are wound up due to stellar rotation. At large distances from the star, the field is essentially toroidal (i.e. has only an azimuthal component). The impact of the magnetic field on the shaping of the shocked wind and the inner nebula is described by the magnetization parameter σ_M , the ratio of magnetic to kinetic energy density of the magnetized stellar wind (see, e.g., Chevalier & Luo 1994):

$$\begin{aligned} \sigma_M &= \frac{B^2}{4\pi\rho v_w^2} = \frac{B_s^2 R_s^2}{\dot{M} v_w} \left(\frac{v_{\text{rot}}}{v_w} \right)^2 \\ &= 7.7 \times 10^{-5} \frac{\left(\frac{B_s}{1 \text{ G}} \right)^2 \left(\frac{R_s}{R_\odot} \right)^2 \left(\frac{v_{\text{rot}}}{v_w} \right)^2}{\left(\frac{\dot{M}}{10^{-8} M_\odot/\text{yr}} \right) \left(\frac{v_w}{1000 \text{ km/s}} \right)}, \end{aligned} \quad (3)$$

where B_s is the magnetic field at the stellar surface, R_s the stellar radius, and \dot{M} and v_w the mass loss rate and the terminal velocity of the central star’s fast wind. Theoretical considerations show that significant deviation from spherical nebular expansion requires a minimum magnetization of the stellar wind given by $\sigma_M \gtrsim 10^{-4}$ (Chevalier & Luo 1994). While the wind is essentially unaffected by the magnetic field at such low values of σ_M , the magnetic pressure becomes significant inside the hot bubble of shocked gas, thus allowing for magnetic shaping of the nebula (see Sect. 4.3).

The condition $\sigma_M \gtrsim 10^{-4}$ can be expressed as

$$B_s \gtrsim B_s^* \approx \frac{(\dot{M}/10^{-8} M_\odot/\text{yr})^{1/2} (v_w/1000 \text{ km/s})^{1/2}}{(R_s/R_\odot) (v_{\text{rot}}/v_w)}, \quad (4)$$

where B_s^* is in units of Gauss.

We compiled the relevant physical parameters of our program stars in Table 3 (except for the four objects whose spectra are dominated by an A-type companion), allowing us to estimate B_s^* according to Eq. (4), assuming $v_{\text{rot}} \approx v \sin i$, or $v_{\text{rot}} \approx 10$ km/s where no measurement of $v \sin i$ is available. For most of the central stars of our sample, B_s^* turns out to be weaker than 100 G (see Table 3). Note that for the central stars of IC 418 and NGC 2392, B_s^* is particularly low because of the high rotational velocity and the low wind speed, respectively.

Assuming that any potential large-scale magnetic field at the surface of the central stars would be dipole-like, we make the statistical approximation $B_s \approx 3 \langle B_z \rangle$. The upper limit of B_s derived from our measurements, $|3 \langle B_z \rangle|$, is listed individually for each target in Table 3 (Col. 9).

We find that, except for two of our targets (NGC 246 and LSS 1362), the upper limit for $\langle B_z \rangle$ that excludes magnetic shaping lies at least a factor of 10 below the upper limit provided by our measurements. For most of our targets, we therefore cannot rule out the presence of a stellar surface magnetic field that is strong enough for shaping the present fast wind of the central stars.

We have to keep in mind, however, that the shaping of the PN must have occurred during a preceding period of time, starting in the early stages of post-AGB evolution. We are therefore interested to know whether the magnetic

field was strong enough to influence the stellar wind when the nebula was just about to form. For this purpose, we extrapolate B_s backward in time, starting at the current value, and assuming that (i) the stellar luminosity is constant, $T_{\text{eff}}^4 R_s^2 = \text{const.}$; (ii) the angular momentum of the star is conserved, $v_{\text{rot}} R_s = \text{const.}$; (iii) the fast wind velocity scales with the escape velocity, $v_w^2 R_s = \text{const.}$; (iv) $\dot{M} = \text{const.}$; and (v) the total magnetic flux is conserved, $B_s R_s^2 = \text{const.}$, implying that σ_M increases strongly during the time evolution as $\sigma_M \sim T_{\text{eff}}^5$.

To ensure that the magnetization parameter σ_M exceeds the critical value of 10^{-4} already at an earlier time, $t = t_0$, the magnetic field strength at the current time, $t = t_1$, must fulfill the condition

$$B_s \gtrsim B_s^\dagger = B_s^* \left(\frac{T_{\text{eff}}(t_1)}{T_{\text{eff}}(t_0)} \right)^{5/2}. \quad (5)$$

In Table 3, we also provide the value of B_s^\dagger for the assumption $T_{\text{eff}}(t_0) = 20$ kK. We see that B_s^\dagger clearly exceeds the upper limit for the measured stellar field strength, $B_s \approx 3 \langle B_z \rangle$, in the case of NGC 246 and LSS 1362, indicating that magnetic shaping is not expected to play any role for these two round / elliptical objects. On the other hand, we find that the upper limit for B_s estimated from our magnetic field measurements is still about a factor of 5 to 10 higher than B_s^\dagger for the five PNe IC 418, NGC 2392, Hen 2-108, Hen 2-113, and Hen 2-131. For these objects, our measurements do not rule out the possibility that their nebulae have been subject to magnetic shaping since early on in their post-AGB evolution when $T_{\text{eff}} \approx 20$ kK, or even since shortly after the end of the AGB evolution (see below). The situation is less clear for NGC 1360 where B_s^\dagger is intermediate between the two extremes mentioned above.

The estimation of the magnetization parameter at even earlier times, near the tip of the AGB ($t = t_{\text{AGB}}$, $T_{\text{eff}} \approx 5$ kK), is more uncertain because the above assumption of constant mass loss rate is no longer valid below $T_{\text{eff}} \approx 20$ kK ($t < t_0$). Assuming instead that \dot{M} decreases by a factor of 100 between $t = t_{\text{AGB}}$ and $t = t_0$, while at the same time v_w increases by a factor of 100, we find that, roughly, $\sigma_M(t_{\text{AGB}})/\sigma_M(t_0) \approx 0.1$, in agreement with the numbers quoted by García-Segura et al. (1999) based on Reid et al. (1979). We conclude that the slow but massive AGB wind is probably unaffected by magnetic shaping as long as $B_s < 10B_s^\dagger$, which is the case for most of our targets. For only two targets, IC 418, and NGC 2392, our measurements do not even rule out a marginal magnetic influence on the very early post-AGB wind.

4.3. Magnetic shaping of the hot bubble

The free wind of the central star is bounded by a strong reverse shock at radius R_1 where the kinetic energy of the wind is thermalized. The shocked wind fills the so-called hot bubble, bounded by the contact discontinuity at outer radius R_2 . The strength of the magnetic field in the immediate pre-shock region, B_p , may be estimated from the stellar surface magnetic field, B_s , as $B_p \sim B_s \times v_{\text{rot}}/v_w \times R_s/R_1$ (e.g., Chevalier & Luo 1994), where v_{rot} and v_w are the (equatorial) rotation velocity of the central star and the outflow velocity of its fast wind, while R_s and R_1 is the radius of the central star and the inner radius of the hot bubble, respectively. Assuming $R_1 = 0.01$ pc, we evaluated

the ratio B_p/B_s for the central stars of our target list. The ratio lies in the range 1.7×10^{-9} to 3.5×10^{-7} . We thus conclude that the strength of magnetic fields in the pre-shock region cannot exceed a few hundred μG . Such fields are too weak to influence the structure of the strong wind shock, however, according to the Chevalier & Luo (1994) model, the magnetic field builds up downstream as a consequence of the compressive flow inside the hot bubble.

The structure of the magnetized hot bubble is illustrated in Fig. 1 of Chevalier (1992) for the quasi-spherical case, assuming $\sigma_M = 0.001$, which is readily applicable to the shocked wind bubbles of PNe. Across the shock, B jumps from the pre-shock value B_p to a post-shock value of $B_X(R_1) \approx 16 \times B_p$. Because of the negative velocity gradient inside the hot bubble, the magnetic flux density increases outwards and rises to $B_X(R_2) \approx 320 \times B_p$ at the outer edge of the hot bubble, assuming that $R_2 \approx 5 \times R_1$.

For sufficiently large σ_M , the magnetic field has a direct dynamical effect on the expansion of the hot bubble. Figure 1 of Chevalier (1992) shows that the magnetic pressure, $B_X^2/8\pi$, can even exceed the thermal gas pressure, $n_e k T$, in the outer parts of large (old) bubbles. At the same time, the magnetic tension gives rise to a non-spherical expansion by reducing the driving force in the equatorial direction, thus leading to an elongated shape in the polar direction. This mechanism is at the heart of the magnetic shaping scenario.

According to the model assumptions made above in Sect. 4.2, the hot bubble of older nebulae are expected to harbor stronger magnetic fields than younger nebulae. For constant R_1 , we find that B_p increases as $B_p \sim T_{\text{eff}}^3$. Since T_{eff} typically increases by a factor of 10 during the post-AGB evolution, B_p would increase roughly by a factor of 1000. Taking into account that at the same time the central cavity expands by roughly a factor of 5 (see, e.g., Fig. 5 of Schönberner et al. 2005), we estimate that B_p is about 200 times larger in old compared to young PNe.

4.4. X-ray emission

According to the order of magnitude estimates given in Sect. 4.3, we may assume, as an upper limit, that the magnetic field varies in the X-ray emitting hot bubble between a few mG near the inner shock up to 100 mG strength near the outer contact discontinuity. Weak magnetic fields of this order of magnitude can easily suppress thermal conduction in the direction perpendicular to their field lines. According to Spitzer (1962), the factor by which the thermal conductivity is reduced in this direction with respect to the conductivity along the field lines (or the field-free case) can be expressed for a pure hydrogen plasma as

$$\frac{D_\perp}{D_\parallel} \approx 7.6 \times 10^{-16} \frac{n_e^2}{T_6^3 B_{\mu\text{G}}^2}, \quad (6)$$

where n_e is the electron density in $[\text{cm}^{-3}]$, T_6 the electron temperature in $[10^6 \text{ K}]$, and $B_{\mu\text{G}}$ the magnetic flux density in units of $[10^{-6} \text{ G}]$ (see also Balbus 1986). In the X-ray emitting cavity ($n_e \approx 10$, $T_6 \gtrsim 10$, $B_{\mu\text{G}} \gtrsim 1$) we obtain $D_\perp/D_\parallel \lesssim 10^{-13}$, indicating that any thermal conduction perpendicular to the magnetic field lines is expected to be very effectively suppressed, even for field strengths that are many orders of magnitude below $1 \mu\text{G}$.

If the magnetic field has a purely toroidal orientation in the X-ray emitting central cavity, thermal conduction in the radial direction should be completely suppressed, even if the field is much weaker than those deduced in our present study. As a consequence, the luminosity of the diffuse X-ray emission should be significantly lower, and the characteristic X-ray temperature should be significantly higher than what is typically found in X-ray observations (see, e.g., Steffen et al. 2008). This dilemma may indicate that the nebular field geometry is different from purely toroidal. Alternatively, other physical mechanisms, such as turbulent mixing due to hydrodynamic instabilities at the contact discontinuity (e.g., Stute & Sahai 2006; Toala & Arthur 2014), may provide an efficient channel for radial heat exchange.

4.5. Central star magnetic field and nebular morphology

Two out of the three bipolar nebulae of our sample harbor a central star with an A-type binary companion (NGC 2346 and Hen 2-36). In these cases, the magnetic field measurement of the central stars proper is impossible due to contamination of their spectrum by the A-type companion. For the central star of the remaining bipolar PN, Hen 2-113, our magnetic field measurements provide marginal support for a magnetic origin of the bipolar nebular structure.

For the central star of the elliptical PN LSS 1362, our analysis showed that magnetic shaping is expected to be unlikely and is at best restricted to the present evolutionary stage. This might indicate that the elliptical shape of LSS 1362 has a non-magnetic background, but the constraints are weak. For the remaining six elliptical PNe, the magnetic shaping hypothesis cannot be constrained by our magnetic field estimates.

The only case where we can rule out significant magnetic shaping is NGC 246. Since this PN is indeed round, there is no reason here to invoke a non-magnetic shaping mechanism. No constraints can be derived for the other round PN, Hen 2-108.

In view of the poor statistics, it is clearly impossible to establish any firm empirical relation between the strength of the central star's magnetic field and the morphological type of the associated planetary nebula. Given the rather low measurement accuracy, we also cannot find any clear inconsistencies that would invalidate the magnetic shaping hypothesis.

4.6. Central star magnetic field and X-ray emission

According to Sect. 4.4, both weak and strong magnetic fields suppress thermal conduction with essentially the same efficiency. From this perspective, we would not expect any correlation between the strength of the stellar magnetic field and the luminosity in diffuse X-rays. However, the thermal structure and density profile of the hot bubble can be significantly altered by the presence of sufficiently strong magnetic fields (cf. Sect. 4.3). Obviously, an empirical verification of a possible relation between stellar magnetic field strength and diffuse X-ray emission is impossible with our sample: only two of the elliptical nebulae show diffuse X-ray emission (IC 418 and NGC 2392) and in both cases only a (rather high) upper limit for the stellar magnetic field could be deduced.

On the other hand, the same two objects suggest that the presence of a central point source of hard X-ray emission is not related to the strength of the stellar magnetic field either. Our measurements indicate that the stellar magnetic field is unlikely to be significantly stronger in NGC 2392 than in IC 418, and yet NGC 2392 harbors an X-ray point source while IC 418 does not, which seems difficult to reconcile with the idea of a magnetic origin of the hard X-ray emission.

5. Conclusions

We have analyzed spectropolarimetric observations of 12 central stars of planetary nebulae carried out at the European Southern Observatory with FORS 2 mounted on the 8-m Antu telescope of the VLT. We find marginal evidence for weak mean longitudinal magnetic fields of about 200 G in the central star of the young elliptical nebula IC 418, and for even weaker magnetic fields of about 100 G in the emission-line spectra of the Wolf-Rayet type central star Hen 2-113 and the weak emission line star Hen 2-131. In general, however, we can only estimate upper limits for the mean longitudinal magnetic fields $|\langle B_z \rangle|$ in the range 120 to 800 G. We conclude that strong magnetic fields exceeding 1 kG are not widespread among PNe central stars.

Some of the observed central stars, including IC 418 and Hen 2-131, show a significant night-to-night spectrum variability of the stellar line profiles, which may be attributed to rotational modulation due to magnetic features or inhomogeneities in the stellar wind. Follow-up monitoring of these targets may be worthwhile to confirm the rotational/magnetic variability and to determine the related timescales.

Interestingly, the hypothesis that planetary nebulae are shaped by magnetic fields is not ruled out by our measurements. Theoretical order of magnitude estimates suggest that even weak magnetic fields well below the detection limit of our measurements are sufficient to contribute to the shaping of the surrounding nebulae throughout their evolution. We have to conclude that, at the present accuracy, the available measurements of central star magnetic fields can neither support nor rule out the magnetic shaping hypothesis for most of our targets. We can only infer for NGC 246 and LSS 1362 that magnetic shaping is not playing any significant role.

The only clear 3σ detection of a 250 G mean longitudinal field is achieved for the A-type companion of the central star of NGC 1514. Even though the mass loss of an A-type star is negligible compared to that of the true central star, the magnetic field of the A-type companion might interact with the wind of the central star. Whether or not such interaction would play any role in shaping the surrounding planetary nebula is unclear. In any case, we can assume that both stars formed and evolved in a common environment. The presence of a magnetic field in the companion of the central star is of great interest in the context of understanding the origin of magnetic fields in A-type stars, since only a few magnetic Ap stars are known to belong to close binary systems.

Acknowledgements. C.S. was supported by funds of DFG (project SCHO 394/29-1) and Land Brandenburg (SAW funds from WGL), and also by funds of PTDESYS-05A12BA1. We thank Martin Wendt for fruitful discussions of statistical methods, and the referee, John

Landstreet, for constructive criticism that led to significant improvement of this paper.

References

- Bagnulo, S., Landstreet, J.D., Fossati, L., & Kochukhov, O. 2012, *A&A*, 538, A129
- Balbus, S.A. 1986, *ApJ*, 304, 787
- Balick, B., & Frank, A. 2002, *ARA&A*, 40, 439
- Blackman, E.G. 2009, In: *IAU Symposium No.259*, Eds. K.G. Strassmeier, A.G. Kosovichev, J.E. Beckman, Vol. 259, p. 35
- Bond, H.E., & Ciardullo, R. 1999, *PASP*, 111, 217
- Chevalier, R.A. 1992, *ApJ*, 397, L39
- Chevalier, R.A., & Luo, D. 1994, *ApJ*, 421, 225
- Ciardullo, R., Bond, H.E., Sipior, M.S., et al. 1999, *AJ*, 118, 488
- Corradi, R.L.M., & Schwarz, H.E. 1995, *A&A*, 293, 871
- De Marco, O., & Crowther, P.A. 1998, *MNRAS*, 296, 419
- De Marco, O. 2009, *PASP*, 121, 316
- Douchin, D., De, M.O., Jacoby, G.H., et al. 2012, In: “SF2A-2012: Proceedings of the Annual meeting of the French Society of Astronomy and Astrophysics”. Eds. S. Boissier, P. de Laverny, N. Nardetto, R. Samadi, D. Valls-Gabaud, H. Wozniak, p. 325
- Drilling, J.S. 1983, *ApJ*, 270, L13
- García-Segura, G., Langer, N., Różyczka, M., & Franco, J. 1999, *ApJ*, 517, 767
- García-Díaz, M.T., López, J.A., García-Segura, G., et al. 2008, *ApJ*, 676, 402
- Gräfener, G., Koesterke, L., Hamann, W.-R. 2002, *A&A*, 387, 244
- Hamann, W.-R., Gräfener, G. 2003, *A&A*, 410, 993
- Heap, S.R. 1977, *ApJ*, 215, 609
- Herald, J.E., & Bianchi, L. 2011, *MNRAS*, 417, 2440
- Hoogerwerf, R., Szentgyorgyi, A., Raymond, J., et al. 2007, *ApJ*, 670, 442
- Hubrig, S., Kurtz, D.W., Bagnulo, S., et al. 2004a, *A&A*, 415, 661
- Hubrig, S., Szeifert, T., Schöller, M., et al. 2004b, *A&A*, 415, 685
- Hubrig, S., Schöller, M., & Kholtygin, A.F. 2014, *MNRAS*, 440, 1779
- Jordan, S., Werner, K., & O’Toole, S.J. 2005, *A&A*, 432, 273
- Jordan, S., Bagnulo, S., Werner, K., & O’Toole, S.J. 2012, *A&A*, 542, A64
- Kastner, J.H., Montez, Jr., R., Balick, B., et al. 2012, *AJ*, 144, 58
- Koesterke, L., Dreizler, S., & Rauch, T. 1998, *A&A*, 330, 1041
- Kudritzki, R.P., Mendez, R.H., Puls, J., & McCarthy, J.K. 1997, *Planetary Nebulae*, 180, 64
- Kudritzki, R.P., Urbaneja, M.A., & Puls, J. 2006, *Planetary Nebulae in our Galaxy and Beyond*, 234, 119
- Lagadec, E., Chesneau, O., Matsuura, M., et al. 2006, *A&A*, 448, 203
- Leitherer, C., & Chavarria-K., C. 1987, *A&A*, 175, 208
- Leone, F., Martínez González, M.J., Corradi, R.L.M., et al. 2011, *ApJL*, 731, L33
- Leone, F., Corradi, R. L. M., Martínez González, M. J., Asensio Ramos, A., & Manso Sainz, R. 2014, *A&A*, 563, A43
- Marten, H., & Schönberner, D. 1991, *A&A*, 248, 590
- Mellema, G. 1994, *A&A*, 290, 915
- Mellema, G. 1995, *MNRAS*, 277, 173
- Mellema, G. 1997, *A&A*, 321, L29
- Mendez, R.H., & Niemela, V.S. 1977, *MNRAS*, 178, 409
- Mendez, R.H., Kudritzki, R.P., Herrero, A., Husfeld, D., & Groth, H.G. 1988, *A&A*, 190, 113
- Mendez, R.H., Kudritzki, R.P., & Herrero, A. 1992, *A&A*, 260, 329
- Morisset, C., & Georgiev, L. 2009, *A&A*, 507, 1517
- Pauldrach, A.W.A., Hoffmann, T.L., & Méndez, R.H. 2004, *A&A*, 419, 1111
- Perinotto, M., Schönberner, D., Steffen, M., & Calonaci, C. 2004, *A&A*, 414, 993
- Phillips, J.P. 2003, *MNRAS*, 344, 501
- Press W.H., Teukolsky S.A., Vetterling W.T., Flannery B.P. 2007, *Cambridge: University Press*, 3rd ed., p. 780 ff
- Prinja, R.K., Massa, D.L., Urbaneja, M.A., & Kudritzki, R.-P. 2012, *MNRAS*, 422, 3142
- Rauch, T., Koeper, S., Dreizler, S., et al. 2003, *IAU Symposium No.215*, Eds. A. Maeder and P.R.J. Eenens, ASP, p. 573 (arXiv:astro-ph/0212163)
- Reid, M.J., Moran, J.M., Leach, R.W., et al. 1979, *ApJ*, 227, L89
- Rivinius T., Szeifert T., Barrera L., Townsend R.H.D., Stefl S., Baade D. 2010, *MNRAS*, 405, L46
- Ruiz, N., Chu, Y.H., Gruendl, R.A., et al. 2013, *ApJ*, 767, 35
- Schönberner, D., Jacob, R., & Steffen, M. 2005, *A&A*, 441, 573
- Soker, N. 2006, *PASP*, 118, 260
- Spitzer, L. 1962, *Physics of Fully Ionized Gases*, New York: Interscience (2nd edition), 1962,
- Steffen, M., & Schönberner, D. 2006, *Planetary Nebulae in our Galaxy and Beyond*, 234, 285
- Steffen, M., Schönberner, D., & Warmuth, A. 2008, *A&A*, 489, 173
- Stute, M., & Sahai, R. 2006, *ApJ*, 651, 882
- Toalá, J. A., & Arthur, S. J. 2014, *MNRAS*, 443, 3486
- Traulsen, I., Hoffmann, A.I.D., Rauch, T., et al. 2005, 14th European Workshop on White Dwarfs, 334, 325
- Tylenda, R., Acker, A., & Stenholm, B. 1993, *A&AS*, 102, 595
- Villaver, E., Manchado, A., & García-Segura, G. 2002, *ApJ*, 581, 1204
- Werner, K., & Herwig, F. 2006, *PASP*, 118, 183

Appendix A: Selected wavelength regions

Wavelength region *all* comprises the entire spectral range, but excludes the nebular [O III] emission lines near 5000 Å and pixels affected by instrumental artifacts, as identified in the null spectra and removed by 3σ clipping. For each object, the spectra shown in Fig. A.1 are plotted over the useful spectral range defined in this way (referred to as wavelength set *all* in this work).

Wavelength region *star* is obtained from wavelength region *all* by excluding additional spectral windows that contain nebular emission lines. The latter could be identified in the original CCD frames in traces located above and below the spectrum of the central star. The spectral regions excluded in this procedure are indicated as horizontal bars 0.2 units below the respective stellar continuum of each object in Fig. A.1.

Appendix B: Deriving $\langle B_z \rangle$ and σ_B from linear regression

The mean longitudinal magnetic field $\langle B_z \rangle$ is derived from the fundamental relation

$$y(\lambda) \equiv \frac{V}{I} = -\frac{g_{\text{eff}} e \lambda^2}{4\pi m_e c^2} \frac{1}{I} \frac{dI}{d\lambda} \langle B_z \rangle \equiv x(\lambda) \langle B_z \rangle \quad (\text{B.1})$$

(cf. Eq. (2) and related text for the definition of the different symbols). For the present analysis, we use the original wavelength scale provided by our pipeline ($\Delta\lambda = 0.75$ Å), avoiding interpolation to finer wavelength steps.

B.1. Method R1

Given the original dataset $\{x_i(\lambda), y_i(\lambda)\}_{i=1,N}$, where N is the total number of considered spectral bins, and assuming that relation (B.1) is valid both for absorption and emission lines, with $g_{\text{eff}} \approx 1.2$, we compute $\langle B_z \rangle$ from linear regression (e.g., Press et al. 2007) as:

$$\langle B_z \rangle = \frac{\overline{xy} - \bar{x}\bar{y}}{\overline{x^2} - \bar{x}^2}, \quad (\text{B.2})$$

where we have defined

$$\begin{aligned} \bar{x} &= \frac{\sum_N w_i x_i}{\sum_N w_i}, \quad \overline{x^2} = \frac{\sum_N w_i x_i^2}{\sum_N w_i}, \\ \bar{y} &= \frac{\sum_N w_i y_i}{\sum_N w_i}, \quad \overline{xy} = \frac{\sum_N w_i x_i y_i}{\sum_N w_i}. \end{aligned} \quad (\text{B.3})$$

The weight of each pixel is given by the square of the signal-to-noise ratio of Stokes V , $w_i = (S/N)_i^2$. Considering the propagation of errors, assuming that the errors in x are negligible, we obtain the formal 1σ uncertainty of $\langle B_z \rangle$ as

$$\begin{aligned} \sigma_B &= \sqrt{\frac{1}{\sum_N w_i} \frac{1}{\overline{x^2} - \bar{x}^2}} \\ &= \frac{1}{\sqrt{N}} \frac{1}{(S/N)_{\text{rms}}} \frac{1}{\sqrt{\overline{x^2} - \bar{x}^2}}. \end{aligned} \quad (\text{B.4})$$

As a sanity check, we also compute the quantity

$$\frac{\chi_{\text{min}}^2}{\nu} = \frac{1}{N-2} \sum_N w_i (y_i - f_i)^2, \quad (\text{B.5})$$

where f_i is the value obtained from the best fitting straight line,

$$f_i = f_0 + \langle B_z \rangle x_i, \quad (\text{B.6})$$

with

$$f_0 = \frac{\overline{x^2 \bar{y}} - \bar{x} \overline{xy}}{\overline{x^2} - \bar{x}^2}. \quad (\text{B.7})$$

Whenever $\chi_{\text{min}}^2/\nu > 1$, σ_B is multiplied by the factor $\sqrt{\chi_{\text{min}}^2/\nu}$ to obtain the final error estimate of $\langle B_z \rangle$. In general, this factor is $\lesssim 1$, and never exceeds 1.07 for the applications considered in this paper.

B.2. Method RM

In this Monte-Carlo type approach, we generate $M = 10^6$ statistical variations of the original dataset $\{x_i(\lambda), y_i(\lambda)\}_{i=1,N}$ by bootstrapping (e.g., Rivinius et al. 2010). Each of the M artificial datasets comprises N data points, obtained by randomly drawing N times a data point from the original sample, assigning the same probability of being drawn to all data points. For each of these M generated datasets, we derive the value $\langle B_z \rangle_m$ using Eq. (B.2), taking the weights w_i of the individual data points into account. The expectation value of $\langle B_z \rangle$ is given by the mean of the distribution,

$$\overline{\langle B_z \rangle} = \frac{1}{M} \sum_{m=1}^M \langle B_z \rangle_m, \quad (\text{B.8})$$

and the 1σ error is estimated from the standard deviation of the distribution, even if the latter is not necessarily Gaussian:

$$\sigma_{\overline{B}} = \sqrt{\frac{1}{M} \sum_{m=1}^M \left(\langle B_z \rangle_m - \overline{\langle B_z \rangle} \right)^2}. \quad (\text{B.9})$$

In this scheme, outliers in the original dataset will automatically translate into an increased error estimate, even if the formal error $(1/\sqrt{w_i})$ assigned to such data points is small.

Appendix C: Error of $\langle B_z \rangle$ from simulated data

Yet another independent estimate of the error margin of our magnetic field measurements is obtained from the following test based on simulated data. Among our targets, we select the [WC]-type central star Hen2-113. With the Potsdam Wolf-Rayet (PoWR) model atmosphere code (Gräfener et al. 2002; Hamann & Gräfener 2003) we calculate a synthetic spectrum that is similar to the observed spectrum of this star. We restrict the normalized synthetic spectrum to the observed wavelength range (4000 – 6000 Å), convolve it with a Gaussian of 3 Å according to the spectral resolution of FORS2, and bin the data to the pixel size of 0.66 Å.

Then we add to the simulated spectrum artificial noise as a Gaussian distribution with a standard deviation equal

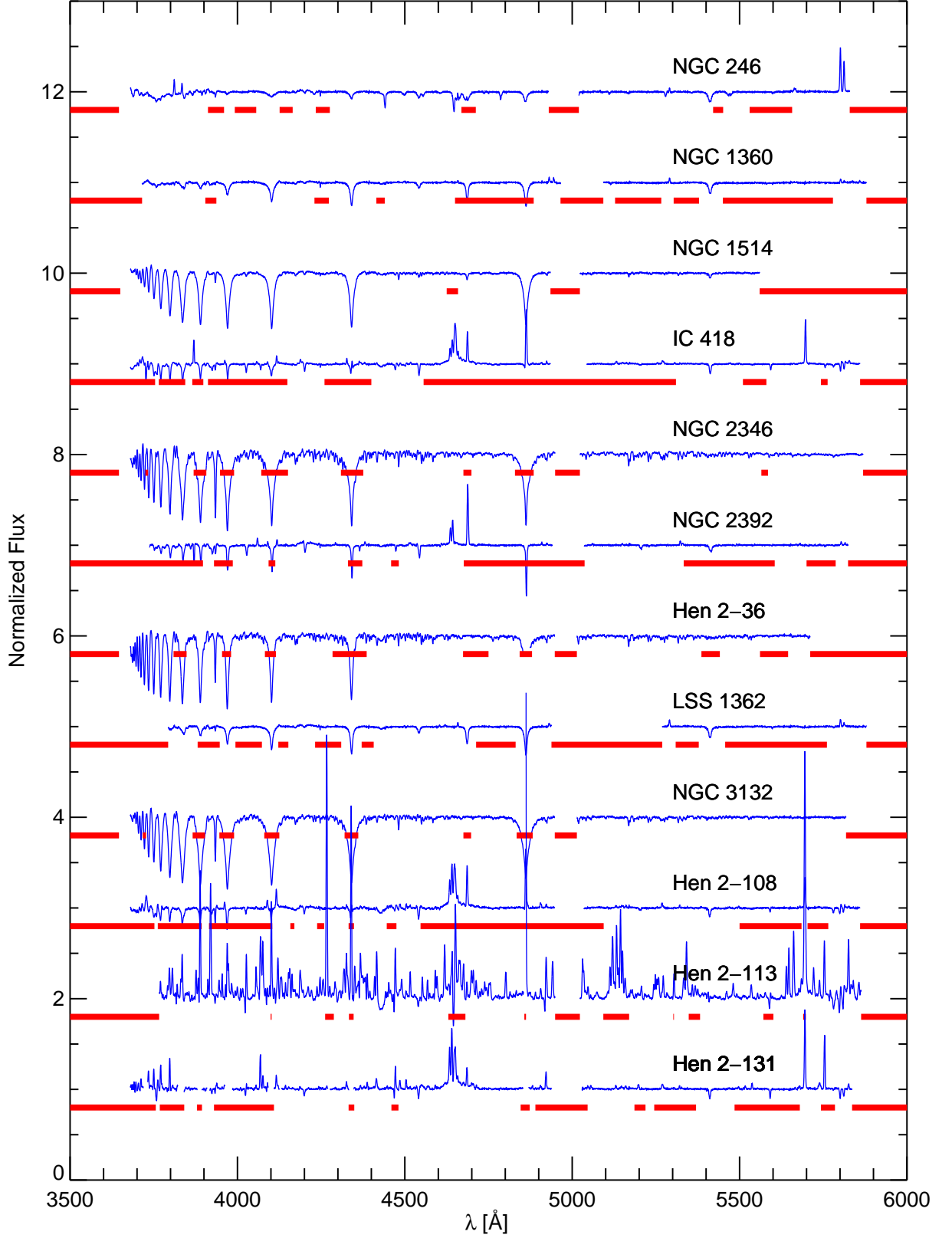


Fig. A.1. Normalized FORS 2 Stokes *I* spectra of the 12 central stars in our sample, displayed with a vertical offset of 1 unit between adjacent spectra. For each object, the displayed spectra (blue) define wavelength set *all* (entire spectrum), gaps indicating the excluded regions, while wavelength set *star* (clean stellar lines only) is obtained by excluding the regions marked by the (red) horizontal bars 0.2 units below the respective stellar continuum.

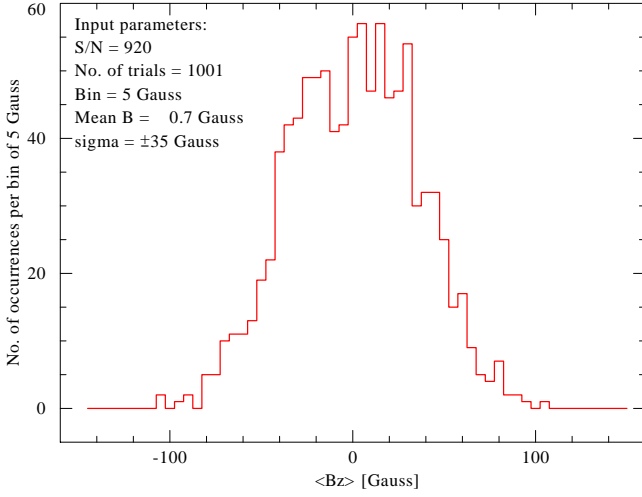


Fig. C.1. Distribution of 1001 $\langle B_z \rangle$ measurements on simulated data for Hen2-113 with input field $\langle B_z \rangle = 0$ and artificial noise corresponding to $S/N = 920$ per pixel in each channel. As the results show, the method has in this case a 1σ error of 35 Gauss.

to SN^{-1} . The signal-to-noise ratio, SN , is set to 920. This corresponds to the quality of our Hen2-113 observations after all spectra from one night that belong to the same polarization channel have been coadded.

Two such simulated spectra with independent statistical noise are now taken to mimic the ordinary and the extraordinary polarization channel, respectively. These data are analyzed for their Zeeman shift in the same way as the real observations. The result is a “measured” field strength $\langle B_z \rangle$. The whole procedure is now repeated 1001 times with the same simulated data, but independent artificial noise. The distribution of the obtained field strength $\langle B_z \rangle$ is plotted as a histogram in Fig. C.1. The obtained $\langle B_z \rangle$ values scatter around zero with a mean deviation of 35 Gauss.

Summarizing, this test was based on the following assumptions: (1) the line spectrum is similar to our simulated, normalized spectrum for Hen2-113; (2) the observed spectra have a S/N ratio of 920 per pixel in the ordinary as well as in the extra-ordinary channel; (3) statistical noise is the only source of errors; (4) both emission and absorption lines are included in the analysis and ‘feel’ the same Zeeman splitting. Under these assumptions, the value obtained for $\langle B_z \rangle$ with FORS2 via our method of analysis has a theoretical 1σ error of ≈ 35 Gauss. Note that this error is independent of the magnetic field strength assumed in modeling the simulated Stokes V spectrum (here $\langle B_z \rangle = 0$).

This exercise suggests that the small formal 1σ error obtained from the actual measurements of Hen2-113 with methods R1 and RM in the range $\sigma_B = 18$ to 30 G is not unrealistic, though it may be somewhat underestimated. Note, however, that a number of lines seen in the observation are missing in the synthetic spectrum.